Assimilation of L-band InSAR snow depth retrievals for improved snowpack quantification

Prabhakar Shrestha[1] and Ana P. Barros[1]

[1]Department of Civil and Environmental Engineering, University of Urbana-Champaign, Urbana, Illinois, USA.

Corresponding Author: Ana P. Barros (barros@illinois.edu)

Abstract

The integration of snow hydrology models and remote sensing observations via data assimilation is a promising method to capture the dynamics of seasonal snowpacks at high spatial resolution and reduce uncertainty with respect to snow water resources. In this study, we employ interferometric Synthetic Aperture Radar (InSAR) technique to quantify snow depth change using modeled snow density and assimilate the referenced and calibrated retrievals into a multilayer snow hydrology model (MSHM). Although the impact of assimilating snow depth change is local in space and time, the impact on snowpack mass properties (snow depth or SWE) is cumulative, and the InSAR retrievals are valuable to improve snowpack simulation and capture the spatial and temporal variability of snow depth or SWE. Details in the estimation algorithm of InSAR snow depth or SWE changes, referencing and calibration prove to be important to minimize errors during data assimilation.

1 Introduction

Remote sensing and distributed modelling of snowpack with data assimilation is a promising methodology to quantify snow water resources (including condition) and reduce uncertainty. Current and upcoming snow remote sensing using Synthetic Aperture Radar (SAR) aim to provide global coverage at hyper-resolution, which is needed to quantify snow variability with reduced uncertainty. Recent studies have either mostly used backscatter approaches (Lievens et al., 2019, 2022; Singh et al., 2024; Tsang et al., 2021) or interferometric SAR (InSAR) techniques(Guneriussen et al., 2001) to quantify snow depth and snow water equivalent (SWE). The latter have been applied extensively for SWE retrievals from dry snowpacks using ground-based (e.g. Leinss et al., 2015; Ruiz et al., 2022)and satellite-based SARs (e.g. Conde et al., 2019; Dagurov et al., 2020; Deeb et al., 2011; Guneriussen et al., 2001; Lei et al., 2023; H. Li et al., 2016; S. Li & Sturm, 2002; Liu et al., 2017). The InSAR technique assumes that the volume backscatter and absorption of microwave signal in the snowpack are negligible with the backscatter at the ground-snowpack interface being dominant while slow propagation of radar waves through snowpack (depending on dielectric property) results in phase delay. Previous studies have shown also that the InSAR retrievals are more suitable at longer wavelengths (e.g., L-band), owing to transparency of dry snow, preservation of coherence for longer periods of time and larger threshold for phase wrapping. With the upcoming NASA-ISRO (Indian Space Research Organization) SAR (NISAR) mission, multiple studies with airborne L-band UAVSAR (Uninhabited Aerial Vehicle Synthetic Aperture Radar) data from 2020 NASA SnowEx campaign have already demonstrated the potential of InSAR for snow remote sensing (e.g. Bonnell et al., 2024; Deeb et al., 2021; Hoppinen et al., 2023; Idowu and Marshall, 2022; Marshall et al., 2021; Palomaki and Sproles, 2023; Tarricone et al., 2022).

86   InSAR retrieval algorithms need spatial data of snow density and referencing to

87   estimate the spatial variability in absolute snow depth or snow water equivalent (SWE).

88   Leinss et al. (2015) have proposed a modified InSAR technique to circumnavigate the

89   need of snow density in SWE retrievals by introducing an additional parameter with

90   very small variability for a range of incidence angles and snow density, their approach

91   also assumes that the vertical profile of snow density does not change between the

92   two dates for each InSAR pair. However, the density profiles can change depending

93   on the time interval between revisits, new snowfall events, and weather conditions that

94   may impact the top layer of the snowpack. Furthermore, snow density might still be

95   needed in referencing the retrievals to obtain absolute snow depth or SWE for

96   assimilation purposes. Hyper-resolution snow hydrology models driven by realistic

97   hydrometeorological forcing can potentially provide a good estimate of for the InSAR

98   algorithm, and in turn the assimilation of InSAR retrievals can potentially improve the

99   modeled snowpack states. Earlier studies have already shown the potential of

100   assimilating retrieval of snow depth or SWE from airborne or satellite SAR to improve

101   modeled snowpack and reduce uncertainty (e.g.Girotto et al., 2024; Pflug et al., 2024;

102   Shrestha and Barros, 2024).The upcoming launch of the NISAR mission that will

103   provide L-band measurements globally provides impetus to investigate the assimilation

104   of InSAR retrievals and associated uncertainty quantification with potential application

105   to operational water prediction. Here, we leverage the multiple in-situ and airborne

106   snow measurements available from NASA's SnowEx'20 (Marshall et al., 2019)

107   campaign over Grand Mesa to 1) evaluate L-band InSAR retrievals of snow depth, and

108   2) assimilate the retrievals into a distributed snow hydrology model to evaluate the

109   impact on the simulated macro-physical snow properties and their uncertainties. We

110   evaluate the L-band InSAR retrievals at their native resolution over different snow

111   depths and land covers against ground-based measurements and airborne Lidar (Light

112 Detection and Ranging) retrievals. The InSAR retrievals with the common first flight

113 date (but different repeat pass) with airborne lidar measurements of snow depth were

114 used for assimilation at different time windows and the other retrievals were used to

115 evaluate the ensemble snow hydrology model prediction of snow properties and to

116 characterize the impact of assimilating the InSAR retrievals of snow depth.

2 Methods

2.1 Study Area

119 The study area is located over the western part of Grand Mesa plateau, Colorado,

120 USA (GM domain; Fig. 1). The land cover is dominated by grassland and mixed forests

121 across the plateau with elevations ranging from 3000 to 3200 m. There are several

122 scattered open water bodies (e.g., lakes and reservoirs), as well as areas with shrubs

123 and wetlands. During the SnowEx'20 campaign, Grand Mesa was used to host an

124 Intensive Observation Period (IOP) during the snow-on season, including bi-weekly

125 UAVSAR flights and airborne Lidar data collections.

2.2 Data

2.2.1 UAVSAR

128 UAVSAR is a fully polarimetric L-band synthetic aperture radar designed to obtain

129 high quality airborne repeat pass interferometry (Hensley et al., 2008; Rosen et al.,

130 2006). The radar operates at a frequency of 1.26 GHz ($\lambda = 0.2379\,m$) with a bandwidth

131 of 80 MHz, and is mounted on the NASA NASA Gulfstream III, flying at a nominal

132 altitude of 13800 m. UAVSAR data are available from the ASF-DAAC for multiple

133 campaigns (https://api.daac.asf.alaska.edu/services/utils/mission_list). The

134 uavsar_pytools (Keskinen et al., 2022;https://github.com/SnowEx/uavsar_pytools)

135   was used to download and convert InSAR georeferenced binary grid files to geotiffs in

136   WGS84 for Grand Mesa (SnowEx'20). The interferometric data consists of the

137   interferogram, coherence, unwrapped phase in quad polarizations, including the digital

138   elevation and incidence angles along the flight path. In some cases, all polarizations

139   were not available. There were 7 InSAR pairs available based on 5 UAVSAR flights for

140   repeated flight paths at a heading of 274° (Table 1). The interval between the InSAR

141   pairs varied between 7 to 40 days (e.g. track 3-5 (11d), 3-8 (18d), 3-13 (25d),3-17

142   (40d),5-8 (7d),8-13 (7d) and 13-17 (15d)).

143   **2.2.2 Snow Pit and Snow Pole Measurements**

144   The snow pit data include measurements of snow temperature, snow depth, snow

145   density, snow stratigraphy, snow grain size, liquid water content, and snow water

146   equivalent over Grand Mesa. The SNEX20_GM_SP collection (Vuyovich et al., 2021)

147   has 154 snow pit measurements between 27 January and 12 February 2020. Similarly,

148   the SNEX20_TS_SP collection(Mason et al., 2024) has time-series of snow pit

149   measurements between October 2019 and May 2020, obtained by the SnowEx

150   community during the 2020 campaign.

151   The snow pole data (SNEX20_SD_TLI**)** consists of snow depth measurements

152   based on time-lapse imagery by capturing a snow pole in each imagery(Breen et al.,

153   2022). The temporal coverage for these data is from 29 September 2019 through 10

154   June 2020. The cameras took either three images daily (11AM, 12 PM, 1PM) or twice

155   daily (11AM and 12PM). The cameras were placed in 9 different environments over the

156   Grand Mesa based on tree-density map (treeless, sparse and dense) and snow depth

157   (shallow, intermediate and deep). The snow depth classification was based on Airborne

158   Snow Observatory (ASO) Lidar retrievals from 8 Feb 2017 .The error estimates for

159   each camera vary and range from ± 2 to ± 16 cm. More details are also available from

160 https://snow.nasa.gov/sites/default/files/users/user354/SNEX-

161 Campaigns/2020/NASASnowEx20_ExperimentPlan_v15.pdf

2.2.3 ASO

163   The Airborne Snow Observatory(ASO; Painter et al., 2016) Lidar derived snow

164 depths at 3 m and 50 m resolution for Grand Mesa were available for Feb 1/2 (fused

165 together) and Feb 13 during the SnowEx'20 campaign. The snow depths over forested

166 area represent snow depths at the ground. SWE estimates were also available from

167 ASO at 50 m resolution, based on bias corrected snow density using a snow hydrology

168 model at 50 m resolution. The reported uncertainty in the data was 5.8 cm and 1.7 cm

169 at 3 m resolution for the two dates, and less than 1 cm at 50 m resolution for both

170 dates. In the ASO retrievals for SWE, the snow density was obtained by calibrating the

171 modelled density with ground-based observations.

2.2.4 Atmospheric data

173   The High-Resolution Rapid Refesh (HRRR;Dowell et al., 2022) 3 km first hour

174 forecast data for water year 2020, was downloaded using a python package(Blaylock,

175 2024;https://doi.org/10.5281/zenodo.4567540). The HRRR ensemble consists of 36

176 members for DA and 9 members for forecast run but were not available in the servers

177 except the single forecast. This HRRR data were used both to estimate atmospheric

178 correction of InSAR phase and as offline atmospheric forcing for the snow hydrology

179 model. The HRRR grids interpolated to regular geographic grids are also outlined in

180 the GM domain (Fig. 1).

2.3 InSAR snow depth retrieval

182   The total interferometric phase difference obtained with repeat pass SAR data

183 over a snow-covered region includes contributions due to phase impacts from flat

184 Earth, local topography, atmospheric delay, snowpack, and random and systematic

185 errors. While the random error mostly comes from the temporal decorrelation,

186 assuming that phase impacts from flat Earth, local topography and systematic errors

187 are accounted for in the UAVSAR InSAR processing chain, the extraction of the phase

188 contribution only requires accurate estimation of phase contribution due to atmospheric

189 delay (see Appendix A1). With known InSAR phase difference ($\Delta\emptyset_s$) due to the

190 presence of snowpack, the change in snow depth (Δz_s) can be estimated following

191 Guneriussen et al. (2001) for coherent reflections:

$$\Delta z_s = -\left(\frac{\lambda}{4\pi}\right)\frac{\Delta\emptyset_s}{\left(cos\theta_i - \sqrt{\varepsilon - sin^2\theta_i}\right)} \tag{1}$$

193 where λ is the SAR wavelength, θ_i is the incidence angle and ε is the bulk

194 snowpack permittivity. For dry snow, $\varepsilon^{"}$ is negligible compared to ε' and the relationship

195 between snow density ρ_s [kgm^{-3}] and permittivity can be expressed according to

196 Matzler, (1996) and Wiesmann and Mätzler (1999) as follows:

$$\varepsilon = 1 + 1.6 * 10^{-3}\rho_s + 1.8 * 10^{-9}\rho_s^3 \tag{2}$$

198 Field measurements of density data are generally sparse and may not be

199 available for all the periods. Also, for future NISAR mission, field measurements alone

200 will not be able to provide the snow density for all grid locations. So, we use modeled

201 snow density (MSHM reference run) driven by atmospheric forcing from an operational

202 numerical weather prediction (NWP), which can be applied everywhere to obtain the

203 bulk snowpack permittivity.

204 Interferometric coherence is important to assess the uncertainty in the retrievals

205 of snow depth, as the retrieval errors increase with decreases in coherence. Ruiz et al.

206 (2022) used a ground based 1-10 GHz SAR system with InSAR capabilities to examine

207 the environmental impact on the observed coherence for snow covered surface. For

208 example, increases in air temperature leading to snow melt are associated with large

209   drops in snow coherence, besides wind, precipitation and large changes in

210   temperature gradients. Compared to X, C and S-band, L-band measurements exhibit

211   higher coherence over longer temporal baselines, and lower error in SWE retrieval,

212   indicating better suitability for InSAR applications.

213   The estimation of Δz_s following Eq. (1) assumes that the density of the snowpack

214   is uniform with depth and that the underlying profile does not change with time. The

215   latter assumption is problematic as the snow density of the underlying profile could

216   change due to physical processes (e.g. compaction) depending on the temporal

217   baseline of the repeat pass and fresh snow. Besides, natural snowpacks are

218   characterized by multi-layer vertical stratigraphy with varying snow density and the

219   phase delay is an integral of the phase delay over the multiple layers (Liens et al.

220   2015). Using $\Delta SWE = \sum_{j=1}^{N} \Delta z_{s,j}\rho_s, j/\rho_w$, where ρ_w is the density of water, and i=1,N

221   are the multiple layers, Liens et al. (2015) proposed a linear relationship between

222   InSAR phase change and SWE change as follows:

223

224
$$\Delta SWE = -\Delta\emptyset_s \left(\frac{\lambda}{2\pi\alpha}\right)\left(1.59 + \theta_i^{\frac{5}{2}}\right)^{-1} \qquad\qquad 3$$

225   where α is an optimal correction factor ranging from $0.92 - 1.07$ for a wide range

226   of incidence angles (up to 65°) and snow densities (up to 900 kgm⁻³). With this

227   formulation and using an optimal α, they estimated a maximum error of 10%. To reduce

228   the uncertainty in snow density, the above method could be directly used to estimate

229   changes in SWE. However, errors due to variations in density profile tied to the

230   temporal baseline between the repeat passes remain to be addressed.

231   Since we evaluate the model results with snow depth measurements from the

232   lidar and ground-based measurements, we employ Eq. 1 for the estimation of snow

233   depth change in this study. Earlier studies (e.g. Bonnell et al., 2024; Marshall et al.,

234   2021; Palomaki and Sproles, 2023) have also used the same approach. Also, InSAR

235   retrievals only provide change in snow depth or SWE, so even for SWE changes, one

236   would require prior SWE measurements or snow depth and snow density to obtain

237   absolute SWE for assimilation. In general, snow depth measurements are more readily

238   available (e.g. lidar or ground measurements) and models with data assimilation can

239   provide close estimate of snow density, so this study also provides a framework for

240   using InSAR snow depth change for data assimilation. Using the atmospherically

241   corrected unwrapped phase images from the UAVSAR data, the snow depth was

242   retrieved over the GM domain in the native grid resolution (approx. 5 m) using average

243   bulk snow density between two repeat pass dates from MSHM reference runs. Note

244   that the estimated change in snow depth is also well below the limit for possible phase

245   wrapping effect in L-band, which is around 69 cm for $\lambda = 23.6\ cm,\ \theta_i = 23°$ and $\rho_s =$

246   $300 kgm^{-3}$ (Deeb et al., 2011). Here, it is also important to note that the estimated

247   change in snow depth is a relative change, and without a snow-free scene or known

248   point change in snow depth, it's not possible to relate the relative change in snow depth

249   to absolute snow depth change. Previous studies (e.g. Bonnell et al., 2024; Conde et

250   al., 2019; Hoppinen et al., 2023; Palomaki and Sproles, 2023; Tarricone et al., 2022)

251   have used different methods (e.g. finding pixels with no changes or using pixels with

252   known changes) to calibrate the InSAR retrievals to obtain absolute change in snow

253   depth or SWE. In this study we use the snow pole measurements over grasslands for

254   the calibration. For cases, where the measurements cannot be collocated due to

255   missing retrievals, we use the snow pole measurement over the sparsely forested

256   areas. In addition, we use an average over a 3x3 square box in the UAVSAR scene to

257   reduce any uncertainty due to GPS location of snow pole measurements. The InSAR

258   snow depth change for a 3x3 square box (native resolution) was compared with snow

259   pole measurements from treeless environment (W1A, W1B and W3A; linearly

interpolated to the time of repeat pass flight) for calibration, and the average value was used for the calibration. For Feb 1-12 retrievals in HV and VH polarization (which had lot of missing data) snow pole measurements from W5A, W6B and W6C were used for calibration. Further, we use VV polarization with higher coherence for spatial evaluation with lidar data, but since it was not available for all retrievals, and HH polarization also exhibit higher coherence and similar results to VV polariztion, HH is used for the InSAR retreivals and data assimilation.

2.4 MPDAF and Experiment Setup

The Multi-Physics Data Assimilation Platform (MPDAFv1.0; Shrestha and Barros, 2024) employs a coupled framework of Multilayer Snow Hydrology Model (MSHMv3.0; Cao and Barros, 2020; Kang and Barros, 2011b, 2011a; Shrestha and Barros, 2024) and the NCAR Data Assimilation Research Testbed (DART; Anderson et al., 2009; DART, 2023). MSHM is a distributed 1D-column model, that solves the mass and energy budgets of the snowpack. Key physical processes of snow hydrology - snow/rain partitioning, snow accumulation, compaction, melting, melt-runoff including snow microstructure evolution are well represented in the model to simulate the macroscopic and microscopic snow properties. The snow microstructure evolution is simulated using a detailed microphysical scheme based on the CROCUS snowpack model (Vionnet et al., 2012). The bottom boundary conditions are kept constant during the cold season assuming frozen soils for snow-on conditions and fixed deep soil temperature. Fresh snow density in this study is based on the parameterization of Hedstrom and Pomeroy (1998) and wet bulb temperature is used as threshold to partition precipitation as rain or snow (Wang et al., 2019). Currently, the rain versus snow partitioning only allows for existence of rain or snow and does not allow for mixed

285 form of rain/snow. More details about the parameterizations can be inferred from the

286 studies mentioned above. Following Cao & Barros (2020), the snow albedo is provided

287 externally using the NLDAS Mosaic Land Surface Model L4 v2.0 albedo data (Xia et

288 al., 2012a; Xia et al., 2012b).

289   In DART, we use the Ensemble Adjustment Kalman Filter (EAKF;Anderson, 2003)

290 with enhanced spatially varying state space inflation (Anderson, 2009; El Gharamti,

291 2018). Assimilation is carried out with observed integrated quantities like total SWE or

292 total snow depth, and the increments are then distributed vertically to the model states

293 (snow depth, snow density and SWE) using a repartition algorithm(Shrestha & Barros,

294 2024).

295   For ensemble Kalman filters, ensemble size fewer than 20-30 can lead to

296 statistical error and larger ensemble size take longer to run with very little benefit. So,

297 30-100 ensemble size is recommended to use with ensemble Kalman filters in DART.

298 In this study, we have only two DART state vectors and use 48 ensemble members

299 which is also constrained by the computational and data storage requirements for

300 hyper-resolution runs. In MSHM, vertically discretized snow depth and SWE are

301 prognostic variables. However, we only use the integrated quantities of these

302 prognostic variables (i.e. total SWE and total snow depth) as state vectors in DART,

303 which are updated by the ensemble filters (e.g. EAKF used here). The ensemble filter

304 assumes a Gaussian relation between the variables in the joint state space prior

305 distribution. First, update increments are computed for each ensemble sample of the

306 observation variable, which is then used to solve for the increments for each state

307 variable. This requires prior cross covariance of each state variable with observation

308 variable along with variance of the observation variable (see Anderson 2003 for

309 details). Then, we use a newly developed repartition algorithm to distribute the

310 increments in the vertical profile with mass conservation (snow density is updated). For

311 bulk or single layer snow hydrology models, such repartitioning is not needed. DA

312 directly impacts the top layers of the snowpack where snow is added or removed based

313 on assimilation increments. The lower layers are only impacted by the modeled snow

314 evolution after the assimilation, primarily due to addition of new layers on top or

315 removal of existing snow layers. The localization setups were used such that the

316 observations only impact model grid points where they are located. The goal is to

317 reduce the impact to surrounding grids with different landcover characteristics, and

318 therefore different retrieval uncertainty such as in the case of forested and non-forested

319 grid points. So, the cutoff radius that determines the region of spatial impact of the

320 assimilated variable was set at approximately 100 m (close to the model resolution).

321   The snow hydrology model is setup over the GM domain using approximately 90

322 m resolution with 66×165 grid points. The maximum number of snow layers in the

323 model was set to 30. The merged atmospheric forcing data are also interpolated to

324 regular geographic grid and disaggregated to 90 m resolution. Here, no downscaling

325 algorithms are applied to the forcing data and the disaggregation technique applies

326 homogeneous forcing over the subgrid pixels – this also allows us to highlight the

327 impact of hyper-resolution data assimilation.

328   The MSHM reference run (CTRL) was integrated from Oct 1, 2019, to Apr 1, 2020

329 using the default HRRR forcing data. For data assimilation (DA) runs, 48 ensemble

330 members were generated by perturbing the model forcing data. The precipitation is

331 perturbed using multiplicative noise drawn from a uniform distribution $U[−0.4, 0.4]$. The

332 incoming shortwave and longwave are also perturbed using a multiplicative noise from

333 a uniform distribution $U[−0.05, 0.05]$ and $U[−0.1, 0.1]$ respectively.

334   Figure 2 synthesizes the availability of ASO Lidar retrievals and L-band InSAR

335 retrievals for assimilation and evaluation of model runs. Here, we use part of the data

336 for assimilation and the remainder are used for evaluation. As stated earlier, the L-band

337 InSAR retrievals only provide information about relative changes in snow depth or

338 SWE, which need to be referenced and calibrated to obtain absolute values needed

339 for assimilation. In the context of distributed modelling at a given resolution, this would

340 require a spatial map of snow depth or SWE for referencing. In this study, we use the

341 ASO Lidar snow depth data at 50 m resolution (Feb 1) as a reference and combine

342 them with aggregated InSAR retrievals of snow depth change I1 (Feb 1-12) , I2 (Feb

343 1-19) and I3 (Feb 1-26) at 50 m resolution to obtain the absolute snow depth pattern

344 over the GM domain on Feb 12, 19 and 26 respectively. Two DA experiments are

345 conducted by assimilating total snow depth: 1) ASO Lidar retrieval on Feb 1, and 2)

346 ASO Lidar retrieval on Feb 1 and referenced InSAR retrievals on Feb 12,19 and 26.

347 We reference the InSAR retrievals by aggregating the data to 50 m resolution grid of

348 the ASO Lidar retrievals from Feb 1, which matches the date of the first InSAR pair in

349 both cases. InSAR retrievals of snow depth change on I5 (Feb 12-19), I6 (Feb 19-26)

350 and I7 (Feb 26-Mar12) are reserved for independent evaluation. In both DA

351 experiments, we assign an observational error of 10 % for the snow depth retrievals at

352 50 m resolution, that is consistent with the errors from the InSAR retrievals using the

353 UAVSAR data in this study.

3   Results

3.1 Meteorological Settings

356 The meteorological conditions based on the HRRR forcing data including air

357 temperature, precipitation and wind speed were analysed for the GM domain (2*5

358 HRRR grids at 3 km resolution). These environmental forcings along with temporal

359 baselines are also the source of variability in interferometric coherence and errors in

360 the retrievals. Figure 3 shows the time-series of air temperature, wind speed and

361   precipitation intensity for the month of February including the first two weeks in March

362   for the NW corner of the GM domain. The month of February was generally cold and

363   windy with temperatures dropping below -20 °C, and wind speeds reaching up to 15

364   m/s. The time-series show cooling and warming periods at a weekly time scale, with

365   some days where the air temperature reached above zero. However, the amplitude of

366   cooling decreases gradually from the end of February to mid-March with more frequent

367   warm periods. There were a few snowfall events between Feb 1-12, Feb 19-26 and

368   Feb 26-Mar 12, which varied in intensity along the GM domain.

369   **3.2 Snow Density**

370   A spatial pattern of bulk snow density is required to compute the snowpack

371   permittivity needed for the InSAR retrieval technique. Uncertainty in snow density

372   estimates can lead to errors in snow depth retrieval. Figure 4 shows the snow density

373   distribution for the InSAR pair (Feb 1-12) using the 50 m resolution ASO Lidar data,

374   snow pit data and model estimates using a reference run (CTRL) for the GM domain.

375   Only the snow pit data within GM domain collected within ± 1 day of the InSAR flights

376   were used for analysis. All three data sets show compaction of snow between the two

377   dates, but the model simulates slightly higher snow density for both flight dates and

378   underestimates the spatial variance as observed in the snow pit data and ASO Lidar

379   data as expected given the coarse resolution of the HRRR precipitation forcing (i.e.

380   3km). Note that the snow density in ASO Lidar data is also from a model estimate but

381   it was bias corrected (i.e., locally calibrated) using the snow pit data from SnowEX'20

382   campaign. In the 11-day temporal baseline, the average snow density changes by

383   5.6 %, 11 % and 4 % respectively among the lidar, snow pit and model data. Here, we

384   have to note that the snow density change in pit data could also be attributed due to

385   spatial variability besides compaction, which could be contributing to higher

386   differences.

387   To examine the error in snow depth retrieval associated with error in density, we

388   used Eq. 1 to retrieve snow depth change for a fixed phase change due to snow. Figure

389   4d shows the variability in InSAR retrieval of snow depth change as a function of

390   incidence angle, for a phase change of -0.17π using the average snow density from

391   ASO Lidar, snow pit and the MSHM CTRL run. The error generally decreases with

392   increasing incidence angle. The synthetic simulation shows that a 10 % error in snow

393   density can lead to approximately 10 % error in snow depth estimates at lower

394   incidence angles, everything else being the same.

395   **3.3 L-band retrieval of snow depth**

396   The temporal baselines for the L-band retrieval range from 7 to 40 days, and the

397   interferometric coherence generally decreased with increasing temporal base lines as

398   expected. For treeless and forested areas, the mean coherence for 7-day temporal

399   baseline (Feb 12-19) was 0.7 ± 0.15 and 0.65 ± 0.18 respectively. Similarly, for the Feb

400   19-26 pair, it was 0.6 ± 0.18 to and 0.5 ± 0.2 respectively. The coherence decreased to

401   0.39 ± 0.16 and 0.36 ± 0.17 for the 40-day temporal baseline. These values are for the

402   HH polarization, as it was available for all dates (see Table 2). The lower coherence

403   for the Feb 19-26 pair compared to Feb 12-19 pair could be attributed to environmental

404   factors, e.g., larger wind speeds, precipitation event, and intermittent warming (see

405   Fig. 3). The forested area exhibits lower coherence than the treeless area suggesting

406   possible higher uncertainty in the retrievals. The above statistics are based on the

407   NLCD landcover data at 30 m resolution, whereas the native resolution of InSAR

408   retrievals from UAVSAR is in the order of 5 m resolution, and the retrievals over forest

409   contain information from snow depth in tree clearings as well.

3.3.1 Evaluation with ASO Lidar data

The InSAR pair of Feb 1-12 with a temporal baseline of 11 days provides the closest concurrent pair with the ASO Lidar retrieval based on Feb1/2 and Feb 13 to compare the snow depth difference at a scale of 3-5 m resolution. Figures 5a-b show the spatial pattern of interferometric coherence and snow depth change at VV polarization. Figure 5c shows the change in snow depth based on ASO Lidar data for the same region. The western part of this GM subdomain is mostly dominated by snow cover over grasslands, while the eastern part contains snow cover in forested areas with relatively lower coherence. Both the Lidar and L-band retrieval capture the wavy roll like pattern due to scouring and drifting of snow over the grasslands shown earlier by Marshall et al. (2021) for a smaller area. Over the eastern part of the subdomain, which is dominated by forest, there are significant discrepancies: in regions with no snow depth change in the ASO Lidar data, a decrease in snow depth is observed in the L-band retrieval.

The average coherence values for this subdomain were 0.51, 0.46, 0.39 and 0.39 for VV, HH, HV and VH polarization respectively. Also, the missing retrievals in the radar scene were 8, 11, 36 and 54 % of the area respectively for the different polarizations (see Table 3). The distribution of snow depth change for co-polarization better matches with the ASO Lidar data compared to cross-polarization (Fig. 5d). The average changes in snow depth for the scene were -2.42, -1.13 and -0.1 cm respectively for ASO Lidar and InSAR VV and HH polarizations. The HV and VH polarization show rightward and leftward shifted peaks respectively. The impact of atmospheric correction was minimal for this retrieval. With and without atmospheric correction, the average snow depth change for the InSAR retrieval (VV) were -1.28 cm and -1.13 cm respectively for the scene. The ASO Lidar and InSAR retrieval are in similar resolution but differ in geolocations, so a quantitative spatial comparison which

436 would require spatial interpolation was not used, but we only explore the patterns and

437 frequency distributions within the same extent. For the frequency distribution (Fig. 5d)

438 between ASO and InSAR (VV), we find R=0.97 and RMSE=2.03 cm, and the previous

439 study (Marshall et al. 2021) found R=0.76, RMSE=4.7cm using the near surface field

440 measured density observations in the retrieval.

441   While the results were similar for other subdomains (not presented here), the L-

442 band retrievals were found to show a general decrease in snow depth in the western

443 most part of GM domain dominated by forest cover, while the Lidar data shows a

444 contrasting increase in snow depth. Thus, the retrievals show higher uncertainty over

445 the forest areas and further evaluation is needed.

446 **3.3.2 Evaluation with snow pole and snow pit time-series data**

447   The snow pole data provide a time-series of snow depth measurements for

448 locations which are treeless or have sparse/dense trees and can be used for

449 comparison with all available InSAR pairs over the GM domain. We use the linearly

450 interpolated snow pole data in time to reference the InSAR retrievals in HH polarization

451 and obtain absolute snow depth for comparison. Figure 6 shows the evaluation of

452 referenced InSAR retrievals with snow pole data for treeless landcover: a-c), sparse

453 trees : d-f), and dense trees : g-m). In most cases, the L-band InSAR retrievals capture

454 the trend in snow depth change very well for different landcover types. The root mean

455 square errors (RMSE) were similar for different landcovers with approximate values of

456 4-6 cm (which is consistent with earlier findings by Marshall et al. (2021) for same

457 InSAR retrieval but different data for evaluation). We also explored the errors in terms

458 of InSAR pairs. The RMSEs of InSAR estimates were 5.0, 4.9, 4.4, 6.2, 7.3 and 4.2 cm

459 respectively for Feb 1-12 (11d), Feb 1-19(18d), Feb 1-26(25d), Feb 12-19(7d), Feb 19-

460 26(7d) and Feb 26-Mar 12(18d) retrievals at the 12 stations. The errors in InSAR

461   retrievals are within 4-8 % of the absolute snow depth.

462   The time-series from snow pits in the north-western part of the GM domain also

463   provide valuable snow depth measurements to evaluate the InSAR estimates. The

464   time-series contains data across treeless and forest areas (Fig. 7). Here, again we use

465   the snow pit measurements to reference the InSAR retrievals and obtain the absolute

466   snow depth. It must be noted that snow pit measurements were carried out at different

467   locations, but within a few meters. Here, we must note that the temporal variability in

468   the snow depth is also partly contributed by the spatial variability due to change in

469   location of pits. The snow depth was slightly higher for the treeless area compared to

470   the forested area, which were within 0.25 km of each other. The InSAR retrievals can

471   capture some of the trends very well, while showing contrasting results for others like

472   for the case of the snow poles. The coherence was within 0.12-0.67 and 0.33-0.79 for

473   the treeless and forested areas, respectively. The errors were 2-9 % and 3-31%

474   respectively for treeless and forest areas. Based on the two comparisons of InSAR

475   retrievals against snow pole and snow pit data, the errors are within 10 % for most of

476   the retrievals with few exceptions.

477   **3.4 Data Assimilation and Evaluation**

478   In this section, we explore the impact of assimilating L-band InSAR retrievals on

479   modeled SWE and particularly modeled snow depth. As already discussed in Section

480   2.4, we use two assimilation experiments including an open loop (without assimilation)

481   and a reference run to explore the time evolution of modeled snowpack over Grand

482   Mesa for the accumulation season in the water year 2020. Figure 8 shows the time-

483   series of spatially averaged modeled snow depth from the different runs. The spatial

484   averaging was done for the grids without trees and open water over the GM domain.

485   The dotted lines indicate the total spread of the ensemble runs. The assimilation of the

ASO lidar snow depth on Feb 1 shifts the ensembles upwards and reduces the spread for both DA and DAU runs. It shows that the reference run (CTRL) was largely underestimating snow depth. While some of the ensemble members with positive perturbation of precipitation of precipitation were able to capture the actual snow depth, the ensembles with negative perturbation of precipitation underestimated the total snow depth (see the spread in OL run). The assimilation of referenced InSAR retrievals for Feb 12, 19 and 26 (DAU runs) exhibit a small increase in snow depth for the ensemble averages compared to DA runs.

The modeled snowpack was also compared with in-situ measurements to assess the impact of data assimilation. The modeled snow depth and SWE at 90 m resolution were compared to snow pit data (IOP and TSD) in locations without trees. The land cover filtered IOP data contained snow depth and SWE from 28 Jan 2020 to 12 Feb 2020. Similarly, the land cover filtered TSD contained snow depth from 19 Dec 2019 to Apr 17, 2020. There were 68 IOP and 12 TSD snow pit data available for comparison across the GM domain based on the model simulation spatial extent. The RMSE decreased from 35.2 cm to 18.3 cm for snow depth, and for SWE it decreased from 8.9 cm to 5.9 cm. The differences in RMSE between DA and DAU runs for these pits were negligible. The modeled snow depth was also compared against snow pole measurements for locations without trees (3 locations, W1A, W1B and W3A) for the entire model simulation period. The RMSE were 17.6, 21.2 and 27.2 cm for the CTRL run, and decreased to 8.1, 21, and 20.8 cm for the DA runs. For DAU runs, the rmse were 8.5, 22.2 and 19.2 cm respectively (see Table 4).

The spatial pattern of the modeled snow depth can be evaluated using the reserved InSAR retrievals from Feb 12-19, Feb 19-26 and Feb 26-Mar12 pairs, that were not used for assimilation. Figure 9 shows the spatial pattern of snow depth change for these repeat pass retrieval dates along with their distribution for the entire

512 GM domain. The estimates are shown for the retrievals and all the model runs. The

513 InSAR data were aggregated to 90 m resolution for comparison. And the grids with

514 open water bodies and tree covers (sparse or dense) were all masked out. Additionally,

515 for the ensemble runs, the spatial maps were obtained by averaging the ensembles,

516 and the distributions are for the averaged ensembles.

517 The InSAR retrievals for Feb 12-19 and Feb 19-26 exhibit both increase and

518 decreases in snow depth for the GM domain, while the retrievals for Feb 26-Mar 12

519 show increase in snow depth only (Fig. 9a-c). As expected, the ensemble average for

520 the open loop (OL) run shows spatial variability at the scale of the atmospheric forcing.

521 The OL run shows similar tendency as InSAR retrievals, except for Feb 12-19 pair,

522 where it shows decrease in snow depth (Fig. 9d-f). While the DA runs improve the total

523 snow depth and SWE, no improvement in the snow depth change is achieved for the

524 Feb 12-19 pair (Fig. 9g). In addition, there are more grids with decrease in snow depth

525 for the remaining two pairs (Fig. 9h-i) compared to the OL run. Note that the DA does

526 increase the modeled spatial variability in snow depth change.

527 Compared to other model runs, DAU produces best results with positive increase

528 in snow depth change (Fig. 9j-k), also seen in the widening of the distribution in the

529 positive direction (Fig. 9m-n). This is due to the assimilation of InSAR data on Feb 19

530 and 26. Since there was no assimilation of InSAR data on Mar 12, there is no

531 improvement in the modeled snow depth change for Feb 26-Mar 12 even in DAU runs

532 (Fig. 9i and Fig. 9l). The increase or relatively larger increase in snow depth change

533 for DAU runs (Fig. 9j-l) are mostly for the grids where the InSAR data were available

534 for assimilation (Feb 19 and Feb 26). However, the impact of this assimilation appears

535 local in time, and it does produce any significant improvement for the Feb 26-Mar 12

536 pair compared to DA runs. Despite the data constraints, these results indicate that the

537 assimilation of InSAR estimates has the potential to improve the spatial pattern of

538   modeled snow depth change. Because the snow depth evolution is accumulative,

539   these changes will impact the overall seasonal evolution of the snowpack.

4   Discussion

541   The hyper-resolution InSAR retrievals resolve the wavy roll like patterns due to

542   scouring and drifting of snow over the grasslands as captured by the ASO lidar data

543   over the grasslands in the NW part of GM domain, also shown earlier by Marshall et

544   al. (2021). However, over forested regions, there are disagreements between the lidar

545   and the InSAR estimates with possible uncertainty in both data sets. The average

546   coherence was similar for VV and HH polarization with slightly higher values for VV

547   polarization and lower for HV and VH polarizations. This resulted in higher percentage

548   of missing retrievals in cross-polarizations. The scene-wide average coherence in HH

549   polarization for the 7-day temporal baseline (treeless area) in the GM domain is around

550   0.6-0.7 which is consistent with values reported by Ruiz et al. (2022). Similarly, the

551   coherence was around 0.5-0.65 for the forested area indicating that the L-band can

552   maintain good coherence over canopy and, with sufficient penetration depending on

553   tree density and canopy architecture, it can be useful in measuring ground snow depth

554   changes. The forested areas generally exhibited lower coherence as expected and the

555   coherence differences between treeless and forested areas were around 14-23% to

556   8 % for 7-day and 40-day temporal baselines, respectively. Overall, the InSAR

557   retrievals generally compare well with in-situ measurements from snow pole and snow

558   pit over sparse and dense forests. RMSE of the lidar measurements over snow pole

559   site used in the study was also around 7-8 cm for the two dates exhibiting good

560   accuracy. So, more data is required for spatial comparison in forested environments to

561   better understand the differences between lidar and InSAR retrievals.

562   The interferometric coherence across the GM domain generally decreased with

563   increasing temporal baseline (e.g. by 44 % from 7 to 40-day temporal baseline). This

564   indicates that the retrieval uncertainty and retrieval error will increase with larger time

565   between the repeat passes as expected. Since the underlying density of snowpack will

566   also change between the repeat passes, the retrieval error will also increase when

567   using a constant density in Eq. 1. In this study, the depth weighted density averages

568   or the average bulk density between two repeat pass dates from the reference MSHM

569   model runs were used for the InSAR retrievals. The reference runs generally

570   underestimated the total snow depth and SWE compared to the ASO lidar data and

571   snow pit measurements, but the bulk snow density was slightly higher than the snow

572   pit observations during the IOP over Grand Mesa. This indicates that the HRRR forcing

573   used for the study underestimates the snowfall events, besides model uncertainty

574   associated with wind redistribution of snow which is not accounted for. The modelled

575   higher bulk density could again indicate uncertainty in the fresh snow density(Cao and

576   Barros, 2020; Shrestha and Barros, 2024) and compaction parameterization (e.g.

577   Abolafia-Rosenzweig et al., 2024). The modelled layered snowpack generally shows

578   a two-layer density profile, with an upper layer exhibiting a gradient and near constant

579   density profile in the lower layer. Upon examining density profiles, the difference in

580   snow density profile in the lower layer varied between 1.5-1.8 % (Feb 19-26) and 6-

581   7 % (Feb 1-26) for 7-day and 25-day temporal baseline. This could be still a lower

582   estimate than the actual change in snow density, as shown earlier for 11-day temporal

583   baseline, which was 4 and 11 % for model and snow pit observations. Therefore, the

584   variability in snow density profiles is small for the 7-day base line, and it is large for 25-

585   day base line during the accumulation period. Besides the modelled density has its

586   own bias compared to actual snowpack density due to forcing and model structural

587   uncertainty. However, the calibration of the retrievals to obtain absolute snow depth

588 change from the relative snow depth change could also compensate for these errors.

589 Further in-depth studies are needed to better understand the sources of error.

590 Data assimilation of the ASO Lidar snow depth reduces the error and uncertainty

591 in the modeled snow depth. This also reduced the bulk snow density for the ensemble

592 members with lower snow depth (compared to CTRL run) by 4-5 %, as new snow with

593 lower density is added on the top by the repartition algorithm (Shrestha and Barros,

594 2024). These ensemble members (DA; Fig. 9h-i) also exhibited lower or negative snow

595 depth change for Feb 19-26 and Feb 26-Mar 12 compared to OL ensembles, which is

596 reflected in the ensemble averages over the GM domain. However, the assimilation of

597 referenced InSAR retrievals (DAU) produces increase in snow depth changes in the

598 ensemble average compared to DA runs. The impact is most apparent in the grids of

599 the GM domain where the data were available for assimilation. This produced the best

600 distribution of snow depth change compared to observations, showing the potential of

601 InSAR retrievals in improving the modeled snowpack. It also demonstrates HRRR

602 underestimation of snowfall between the dates of the InSAR pairs (e.g. between Feb

603 26 and Mar 12) and it explains the small snow depth differences in the OL runs

604 compared to InSAR retrievals. The OL shows the increase in snow depth due to

605 snowfall just before Mar 12 (see Fig. 3) albeit underestimated as indicated by the

606 difference in magnitude between the InSAR retrievals and the OL snow depth changes.

607 Likewise, the impact of assimilating InSAR retrievals which improves the simulated

608 snow depth changes (as seen for the first two pairs) highlights the need for high

609 temporal resolution of SAR measurements.

610 **5 Conclusion**

611 This study shows that InSAR retrievals are useful to improve the snowpack

612   simulation and capture its spatial and temporal variability. The assimilation of hyper-

613   resolution retrievals of snow depth is equivalent to a downscaling of precipitation

614   forcing with a bias correction. The RMSE of the InSAR retrievals of absolute snow

615   depth change at native resolution compared to snow pole measurements over different

616   land covers were within 4-6 cm, which corresponds to less than 10 % of the absolute

617   snow depth. However, reference snow depth or SWE is essential to obtain absolute

618   snow depth or SWE for assimilation purposes, which poses a challenge in an

619   operational context. In this situation, one would start from snow-free conditions and

620   build up the absolute snow depth from InSAR retrievals using the prior estimates as

621   reference. Accurate calibration of the estimated relative snow depth change, or SWE

622   will be important to minimize retrieval errors. Further work is also essential for InSAR

623   retrievals in forested areas and complex terrains. Future studies are needed to

624   advance a general framework for calibrating InSAR retrievals and obtaining absolute

625   snow depth or SWE for assimilation into the models.

626

Code availability

The MPDAF v1.0 software with experiment setups is available from https://github.com/mpdaf23/mpdaf.git. MSHM v3.0 used here is documented in Kang and Barros (2011a, 2011b); Cao and Barros (2020) including the updates described in this paper. MEMLS can be downloaded from http://www.iapmw.unibe.ch/research/projects/snowtools/memls.html. The NCAR DART can be downloaded from https://github.com/NCAR/DART.git.

Data availability

The NASA SnowEx 2020 observation data can be downloaded from NASA National Snow and Ice Data Center Distributed Active Archive Center and ASF DAAC. HRRR atmospheric forcing data can be now downloaded from Amazon Web Services (AWS) courtesy of National Oceanic and Atmospheric Administration (NOAA) and the Registry of Open Data on AWS. The NLDAS albedo data can be downloaded from the NASA GES DISC. Model data and software used for visualization is available from https://uofi.box.com/v/InSARmodeldata.

Author contribution

PS and APB conceptualized the study. PS designed the study, processed the data, conducted the model simulation with data assimilation, carried out the analysis, and wrote the paper. APB acquired the grant for the study and contributed to editing of the manuscript.

Competing interests

The authors declare that they have no conflict of interest.

Acknowledgements

654

655

656   The funding for this study was provided by the National Oceanic and Atmospheric

657   Administration (NOAA), awarded to the Cooperative Institute for Research on

658   Hydrology (CIROH) through the NOAA Cooperative Agreement with The University of

659   Alabama, NA22NWS4320003. This study made use of the Illinois Campus Cluster, a

660   computing resource that is operated by the Illinois Campus Cluster Program (ICCP) in

661   conjunction with the National Center for Supercomputing Applications (NCSA) and

662   which is supported by funds from the University of Illinois at Urbana-Champaign. The

663   analysis of data was done using the NCAR Command Language (Version 6.6.2). We

664   would like to particularly acknowledge the NASA SnowEx campaign including the field

665   and airborne crews who collected the data used in this study. We also acknowledge

666   the collaboration in SnowEx Hackweek which led to the development of multiple tools

667   for downloading and processing data used in this study. The data used in this effort

668   were acquired as part of the activities of NASA's Science Mission Directorate and are

669   archived and distributed by the Goddard Earth Sciences (GES) Data and Information

670   Services Center (DISC).

671

References

Abolafia-Rosenzweig, R., He, C., Chen, F., and Barlage, M.: Evaluating and enhancing snow compaction process in the Noah-MP land surface model, J Adv Model Earth Syst, 16, e2023MS003869, 2024.

Anderson, J.: Spatially and temporally varying adaptive covariance inflation for ensemble filters, Tellus A: Dynamic meteorology and oceanography, 61, 72–83, 2009.

Anderson, J., Hoar, T., Raeder, K., Liu, H., Collins, N., Torn, R., and Avellano, A.: The data assimilation research testbed: A community facility, Bull Am Meteorol Soc, 90, 1283–1296, 2009.

Anderson, J. L.: A local least squares framework for ensemble filtering, Mon Weather Rev, 131, 634–642, 2003.

Blaylock, B. K.: Herbie: Retrieve Numerical Weather Prediction Model Data, https://doi.org/10.5281/zenodo.13329302, August 2024.

Bonnell, R., McGrath, D., Tarricone, J., Marshall, H.-P., Bump, E., Duncan, C., Kampf, S., Lou, Y., Olsen-Mikitowicz, A., and Sears, M.: Evaluating L-band InSAR Snow Water Equivalent Retrievals with Repeat Ground-Penetrating Radar and Terrestrial Lidar Surveys in Northern Colorado, EGUsphere, 2024, 1–33, 2024.

Breen, C. M., Hiemstra, C., Vuyovich, C. M., and Mason, M.: SnowEx20 Grand Mesa Snow Depth from Snow Pole Time-Lapse Imagery, Version 1, Boulder, Colorado USA, 2022.

Cao, Y. and Barros, A. P.: Weather-dependent nonlinear microwave behavior of seasonal high-elevation snowpacks, Remote Sens (Basel), 12, 3422, 2020.

Conde, V., Nico, G., Mateus, P., Catalão, J., Kontu, A., and Gritsevich, M.: On the estimation of temporal changes of snow water equivalent by spaceborne SAR interferometry: a new application for the Sentinel-1 mission, Journal of Hydrology and

698   Hydromechanics, 67, 93–100, 2019.

699   Dagurov, P. N., Chimitdorzhiev, T. N., Dmitriev, A. V, and Dobrynin, S. I.:

700   Estimation of snow water equivalent from L-band radar interferometry: simulation and

701   experiment, Int J Remote Sens, 41, 9328–9359, 2020.

702   DART: The data assimilation research testbed (version 10.7.3), Boulder,

703   Coloardo, 2023.

704   Deeb, E., Forster, R., Vuyovich, C., Elder, K., Hiemstra, C., and Lund, J.: L-band

705   InSAR depth retrieval during the NASA SnowEx 2020 campaign: Grand mesa,

706   Colorado, in: 2021 IEEE International Geoscience and Remote Sensing Symposium

707   IGARSS, 625–627, 2021.

708   Deeb, E. J., Forster, R. R., and Kane, D. L.: Monitoring snowpack evolution using

709   interferometric synthetic aperture radar on the North Slope of Alaska, USA, Int J

710   Remote Sens, 32, 3985–4003, 2011.

711   Dowell, D. C., Alexander, C. R., James, E. P., Weygandt, S. S., Benjamin, S. G.,

712   Manikin, G. S., Blake, B. T., Brown, J. M., Olson, J. B., and Hu, M.: The High-Resolution

713   Rapid Refresh (HRRR): An hourly updating convection-allowing forecast model. Part

714   I: Motivation and system description, Weather Forecast, 37, 1371–1395, 2022.

715   El Gharamti, M.: Enhanced adaptive inflation algorithm for ensemble filters, Mon

716   Weather Rev, 146, 623–640, 2018.

717   Girotto, M., Formetta, G., Azimi, S., Bachand, C., Cowherd, M., De Lannoy, G.,

718   Lievens, H., Modanesi, S., Raleigh, M. S., and Rigon, R.: Identifying snowfall elevation

719   patterns by assimilating satellite-based snow depth retrievals, Science of The Total

720   Environment, 906, 167312, 2024.

721   Guneriussen, T., Hogda, K. A., Johnsen, H., and Lauknes, I.: InSAR for estimation

722   of changes in snow water equivalent of dry snow, IEEE Transactions on Geoscience

723   and Remote Sensing, 39, 2101–2108, 2001.

724   Hanssen, R. F.: Radar interferometry: data interpretation and error analysis,

725   Springer Science & Business Media, 2001.

726   Hensley, S., Wheeler, K., Sadowy, G., Jones, C., Shaffer, S., Zebker, H., Miller,

727   T., Heavey, B., Chuang, E., and Chao, R.: The UAVSAR instrument: Description and

728   first results, in: 2008 IEEE Radar Conference, 1–6, 2008.

729   Hoppinen, Z. M., Oveisgharan, S., Marshall, H.-P., Mower, R., Elder, K., and

730   Vuyovich, C.: Snow Water Equivalent Retrieval Over Idaho, Part B: Using L-band

731   UAVSAR Repeat-Pass Interferometry, The Cryosphere Discussions, 2023, 1–24,

732   2023.

733   Idowu, A. N. and Marshall, H.-P.: Snow depth retrieval from L-band data based

734   on repeat pass InSAR techniques, in: IGARSS 2022-2022 IEEE International

735   Geoscience and Remote Sensing Symposium, 4248–4251, 2022.

736   Kang, D. H. and Barros, A. P.: Observing system simulation of snow microwave

737   emissions over data sparse regions—Part I: Single layer physics, IEEE transactions

738   on geoscience and remote sensing, 50, 1785–1805, 2011a.

739   Kang, D. H. and Barros, A. P.: Observing system simulation of snow microwave

740   emissions over data sparse regions—Part II: Multilayer physics, IEEE transactions on

741   geoscience and remote sensing, 50, 1806–1820, 2011b.

742   Keskinen, Z., Tarricone, J., Surfix, and Marshall, H.: SnowEx/uavsar_pytools:

743   v0.2.0, https://doi.org/10.5281/zenodo.6578193, May 2022.

744   Lei, Y., Shi, J., Liang, C., Werner, C., and Siqueira, P.: Snow Water Equivalent

745   Retrieval Using Spaceborne Repeat-Pass L-Band SAR Interferometry Over Sparse

746   Vegetation Covered Regions, in: IGARSS 2023-2023 IEEE International Geoscience

747   and Remote Sensing Symposium, 852–855, 2023.

748   Leinss, S., Wiesmann, A., Lemmetyinen, J., and Hajnsek, I.: Snow water

749   equivalent of dry snow measured by differential interferometry, IEEE J Sel Top Appl

750 Earth Obs Remote Sens, 8, 3773–3790, 2015.

751 Li, H., Xiao, P., Feng, X., He, G., and Wang, Z.: Monitoring snow depth and its

752 change using repeat-pass interferometric SAR in Manas River Basin, in: 2016 IEEE

753 International Geoscience and Remote Sensing Symposium (IGARSS), 4936–4939,

754 2016.

755 Li, S. and Sturm, M.: Patterns of wind-drifted snow on the Alaskan arctic slope,

756 detected with ERS-1 interferometric SAR, Journal of Glaciology, 48, 495–504, 2002.

757 Lievens, H., Demuzere, M., Marshall, H.-P., Reichle, R. H., Brucker, L., Brangers,

758 I., de Rosnay, P., Dumont, M., Girotto, M., and Immerzeel, W. W.: Snow depth variability

759 in the Northern Hemisphere mountains observed from space, Nat Commun, 10, 4629,

760 2019.

761 Lievens, H., Brangers, I., Marshall, H.-P., Jonas, T., Olefs, M., and De Lannoy,

762 G.: Sentinel-1 snow depth retrieval at sub-kilometer resolution over the European Alps,

763 Cryosphere, 16, 159–177, 2022.

764 Liu, Y., Li, L., Yang, J., Chen, X., and Hao, J.: Estimating snow depth using multi-

765 source data fusion based on the D-InSAR method and 3DVAR fusion algorithm,

766 Remote Sens (Basel), 9, 1195, 2017.

767 Marshall, H. , V. C. , H. C. , B. L. , E. K. , D. J. , and N. J.: NASA SnowEx 2020

768 Experiment Plan, 2019.

769 Marshall, H.-P., Deeb, E., Forster, R., Vuyovich, C., Elder, K., Hiemstra, C., and

770 Lund, J.: L-band InSAR depth retrieval during the NASA SnowEx 2020 campaign:

771 Grand mesa, Colorado, in: 2021 IEEE International Geoscience and Remote Sensing

772 Symposium IGARSS, 625–627, 2021.

773 Mason, M., Marshall, H., McCormick, M., Craaybeek, D., Elder, K., and Vuyovich,

774 C. M.: SnowEx20 Time Series Snow Pit Measurements, Version 2, Boulder, Colorado

775 USA, 2024.

776   Matzler, C.: Microwave permittivity of dry snow, IEEE Transactions on

777   Geoscience and Remote Sensing, 34, 573–581, 1996.

778   Painter, T. H., Berisford, D. F., Boardman, J. W., Bormann, K. J., Deems, J. S.,

779   Gehrke, F., Hedrick, A., Joyce, M., Laidlaw, R., and Marks, D.: The Airborne Snow

780   Observatory: Fusion of scanning lidar, imaging spectrometer, and physically-based

781   modeling for mapping snow water equivalent and snow albedo, Remote Sens Environ,

782   184, 139–152, 2016.

783   Palomaki, R. T. and Sproles, E. A.: Assessment of L-band InSAR snow estimation

784   techniques over a shallow, heterogeneous prairie snowpack, Remote Sens Environ,

785   296, 113744, 2023.

786   Pflug, J. M., Wrzesien, M. L., Kumar, S. V, Cho, E., Arsenault, K. R., Houser, P.

787   R., and Vuyovich, C. M.: Extending the utility of space-borne snow water equivalent

788   observations over vegetated areas with data assimilation, Hydrol Earth Syst Sci, 28,

789   631–648, 2024.

790   Rosen, P. A., Hensley, S., Wheeler, K., Sadowy, G., Miller, T., Shaffer, S.,

791   Muellerschoen, R., Jones, C., Zebker, H., and Madsen, S.: UAVSAR: A new NASA

792   airborne SAR system for science and technology research, in: 2006 IEEE conference

793   on radar, 8-pp, 2006.

794   Ruiz, J. J., Lemmetyinen, J., Kontu, A., Tarvainen, R., Vehmas, R., Pulliainen, J.,

795   and Praks, J.: Investigation of environmental effects on coherence loss in SAR

796   interferometry for snow water equivalent retrieval, IEEE Transactions on Geoscience

797   and Remote Sensing, 60, 1–15, 2022.

798   Shrestha P. and A . P. Barros: Multi-physics Data Assimilation Framework for

799   Remotely Sensed Snowpacks to Improve Water Prediction, Water Resource

800   Research, 2024.

801   Singh, S., Durand, M., Kim, E., and Barros, A. P.: Bayesian physical–statistical

802 retrieval of snow water equivalent and snow depth from X-and Ku-band synthetic

803 aperture radar–demonstration using airborne SnowSAr in SnowEx'17, Cryosphere, 18,

804 747–773, 2024.

805 Smith, E. K. and Weintraub, S.: The constants in the equation for atmospheric

806 refractive index at radio frequencies, Proceedings of the IRE, 41, 1035–1037, 1953.

807 Tarricone, J., Webb, R. W., Marshall, H.-P., Nolin, A. W., and Meyer, F. J.:

808 Estimating snow accumulation and ablation with L-band InSAR, The Cryosphere

809 Discussions, 2022, 1–33, 2022.

810 Tsang, L., Durand, M., Derksen, C., Barros, A. P., Kang, D.-H., Lievens, H.,

811 Marshall, H.-P., Zhu, J., Johnson, J., and King, J.: Global monitoring of snow water

812 equivalent using high frequency radar remote sensing, The Cryosphere Discussions,

813 2021, 1–57, 2021.

814 Vuyovich, C., H.P. Marshall, K. Elder, C. Hiemstra, L. Brucker, and M. McCormick:

815 SnowEx20 Grand Mesa Intensive Observation Period Snow Pit Measurements,

816 Version 1, NASA National Snow and Ice Data Center Distributed Active Archive Center,

817 2021.

818 Wang, X., Zeng, Q., and Jiao, J.: Utilization of WRF 3D Meteorological Data to

819 Calculate Slant Total Delay for InSAR Atmospheric Correction, Remote Sens Earth

820 Syst Sci, 4, 30–43, 2021.

821 Wiesmann, A. and Mätzler, C.: Microwave emission model of layered snowpacks,

822 Remote Sens Environ, 70, 307–316, 1999.

823 Xia, Y., Mitchell, K., Ek, M., Cosgrove, B., Sheffield, J., Luo, L., Alonge, C., Wei,

824 H., Meng, J., and Livneh, B.: Continental-scale water and energy flux analysis and

825 validation for North American Land Data Assimilation System project phase 2 (NLDAS-

826 2): 2. Validation of model-simulated streamflow, Journal of Geophysical Research:

827 Atmospheres, 117, 2012a.

828   Xia, Y., Mitchell, K., Ek, M., Sheffield, J., Cosgrove, B., Wood, E., Luo, L., Alonge,

829   C., Wei, H., and Meng, J.: Continental-scale water and energy flux analysis and

830   validation for the North American Land Data Assimilation System project phase 2

831   (NLDAS-2): 1. Intercomparison and application of model products, Journal of

832   Geophysical Research: Atmospheres, 117, 2012b.

833

834

Appendix A1

835

836

837 The atmospheric delay experienced by a microwave signal can be estimated by

838 integrating the atmospheric refractivity along the line of sight from the surface to the

839 airborne sensor height. Neglecting the impact of ionosphere for the UAVSAR flying at

840 a height of z_s, the scaled up atmospheric refractivity of moist air [N=(n-1)10^6], where n

841 is the refractive index, is given by

842
$$N(x,z) = k_1 \frac{P}{T} + (k_2 - k_1)\frac{e}{T} + k_3 \frac{e}{T^2} + k_4 W_{cl}$$

843 where P is pressure [hPa], T is air temperature [K], e is vapor pressure [hPa], W_{cl}

844 is liquid water content [kgm^{-3}], n_e is ionization and f is frequency. The remaining term

845 are constants: $k_1 = 0.776\ KPa^{-1}$, $k_2 = 0.716\ KPa^{-1}$, $k_3 = 3750\ K^2 Pa^{-1}$, $k_4 = $

846 $1430\ m^3 kg^{-1}$. Based on the works of Smith and Weintraub (1953), the above relation

847 is restricted to certain limits of the variables for an accuracy of 0.5 percent in N(x,z).

848 The limits in this case restrict its use to temperatures of -50 to + 40° C, total pressures

849 of 200 to 1100 mb, water-vapor partial pressures of 0 to 30 mb, and a frequency range

850 of 0 to 30 GHz.

851 $N(x,z)$ can be further decomposed into the mean and turbulent part for a radar

852 scene as:

853
$$N(x,z) = \bar{N}(z) + N'(x,z)$$

854 where $\bar{N}(z)$ is the average vertical stratification for the given resolution of the

855 atmospheric model (here 3 km) and $N'(x,z)$ is the deviation from the average profile

856 along the location x in the radar scene (within the atmospheric grid). Neglecting the

857 turbulent terms, zenith delay L for the mean part can be computed as

858
$$L = \int_{z_{ref}}^{z_s} \left(k_1 \frac{P}{T} + (k_2 - k_1)\frac{e}{T} + k_3 \frac{e}{T^2} \right) dz$$

859 Using $dP = -\rho g dz$ and $\rho = P/R_d T$, where ρ is air density [kgm^{-3}] , $R_d = $

860    $287.053 \, Jkg^{-1}K^{-1}$ is the dry gas constant, ang g is acceleration due to gravity, we

861   obtain:

862
$$L = -10^{-6}\left(k_1\frac{R_d}{g}\left(P(z_s) - P(z_{ref})\right)\right) + 10^{-6}\int_{z_{ref}}^{z_s}\left((k_2 - k_1)\frac{e}{T} + k_3\frac{e}{T^2}\right)dz$$

863   The first term of the right side is the hydrostatic correction term, and the second

864   term is the wet correction term. The atmospheric phase delay along the line of sight

865   (LOS) can then be estimated using the microwave wavelength (λ) and incidence angle

866   (θ_{inc}) as:

867
$$\emptyset_{atm} = \frac{4\pi}{\lambda}\frac{L}{\cos(\theta_{inc})}$$

868   The above simple approximation for computing atmospheric phase delay along

869   the LOS could introduce additional uncertainty(Wang et al., 2021). More importantly,

870   since SAR interferograms are not sensitive to image-wide phase biases, there will be

871   no horizontal delay differences over flat terrain. However, for a radar scene with terrain,

872   the differences in the vertical refractivity during both acquisitions will affect phase

873   difference between two arbitrary resolution cells with different topographic

874   height(Hanssen, 2001). Therefore, the contribution of tropospheric stratification in the

875   interferogram will only be present if the radar scene has resolution cells with different

876   elevations. So, we compute the differential atmospheric phase delay between location

877   with maximum elevation ($z_{ref} = p$) and all other locations ($z_{ref} = q$) in the radar scene

878   for two SAR acquisition time t_1 and t_2 as:

879
$$\Delta\emptyset_{atm} = \frac{4\pi}{\lambda cos\theta_{inc}}\left[(L_p^{t_1} - L_q^{t_1}) - (L_p^{t_2} - L_q^{t_2})\right]$$

880   Then the phase change contribution due to snowpack is estimated as:

881
$$\Delta\emptyset_s = \Delta\emptyset_{InSAR} - \Delta\emptyset_{atm}$$

882

Tables

Table 1: UAVSAR flight retrieval dates for Grand Mesa during SnowEx'20 campaign.

Flight track	Acquisition Date
3	Feb 01 2020 (02:13:36 – 02:15:58 UTC)
5	Feb 12 2020 (16:47:20 – 16:49:45 UTC)
8	Feb 19 2020 (17:24:18 – 17:27:07 UTC)
13	Feb 26 2020 (17:40:54 – 17:43:34 UTC)
17	Mar 12 2020 (18:17:08 – 18:20:28 UTC)

Table 2: Coherence for treeless and forested environment for different retrievals.

	Period (days)	Coherence (HH)	
		Treeless	Forested
Feb 12-19	7	0.71 ± 0.15	0.65 ± 0.18
Feb 19-26	7	0.6 ± 0.18	0.5 ± 0.2
Feb 1-12	11	0.48 ± 0.18	0.47 ± 0.19
Feb 26 – Mar 12	15	0.49 ± 0.17	0.39 ± 0.18
Feb 1-19	18	0.47 ± 0.18	0.43 ± 0.19
Feb 1-26	25	0.46 ± 0.18	0.43 ± 0.18
Feb 1- Mar 12	40	0.39 ± 0.16	0.36 ± 0.17

Table 3: InSAR retrievals of snow depth change at different polarization for Feb 1-12

Polariation	Coherence	% missing	Avg. Change (cm)
VV	0.51	8	-1.13
HH	0.46	11	-0.1
HV	0.39	36	2.61
VH	0.39	54	-2.67

Table 4: Root mean square error for modeled snow depth (cm) over treeless environments with reference to pit (IOP and TSD) and snow pole measurements.

	Pit	W1A	W1B	W3A
CTRL	35.2	17.6	21.2	27.2
OL	36.0	11.57	14.80	30.8
DA	18.3	8.1	21	20.8
DAU	18.0	8.5	22.2	19.2

896 **Figures**
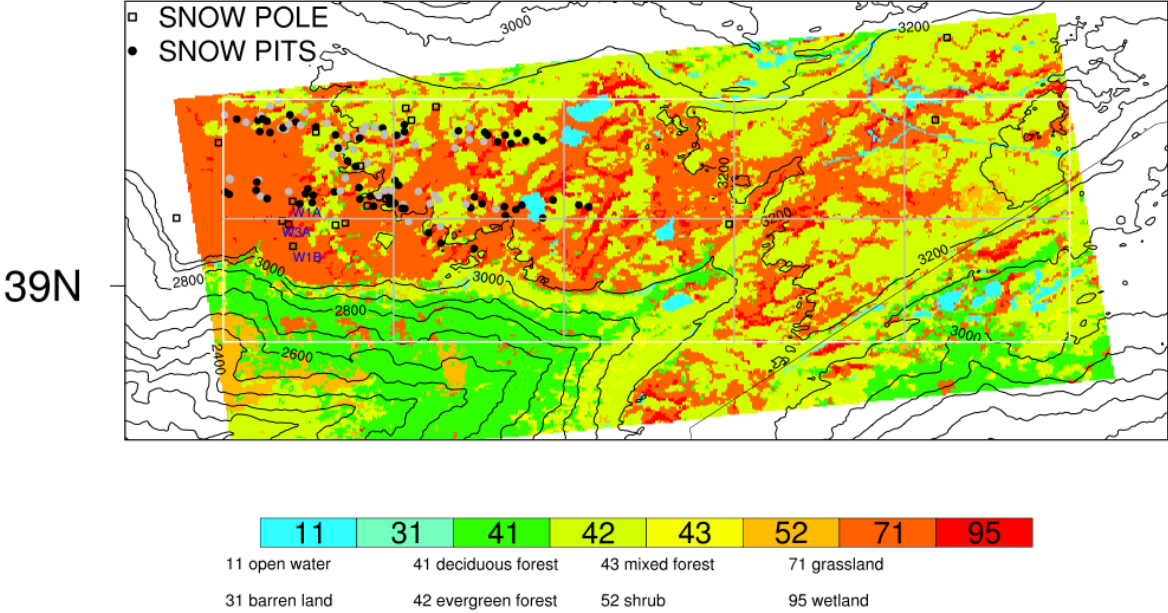
897

898

899 **Figure 1:** Spatial pattern of land cover and topography over the Grand Mesa (GM)

900 domain (white outline). The gray boxes outline the 3 km atmospheric grids. The solid

901 black/gray and square markers show the location of snow pit and snow pole

902 measurements available from SnowEx'20 campaign. The snow pole measurements

903 used for calibration of InSAR retrievals are also highlighted with their names.

904
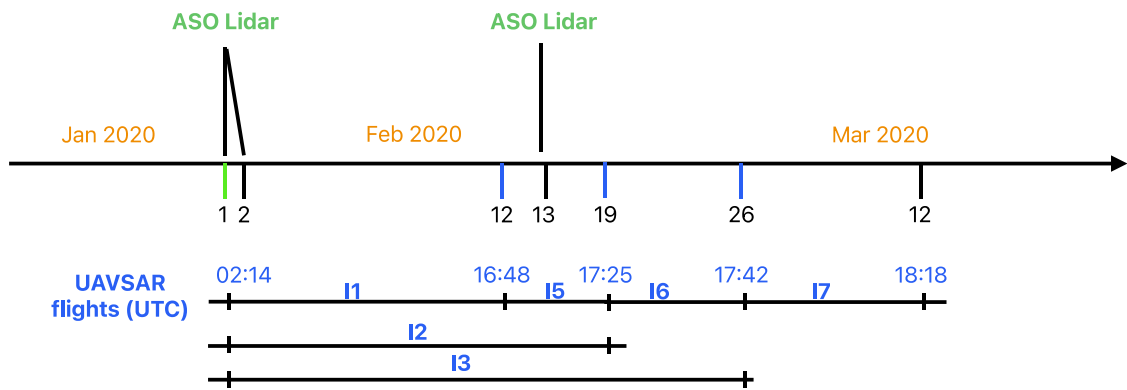
Figure 2: Timeline of availability of UAVSAR interferometric products and ASO Lidar retrievals of snow depth and SWE for SnowEx'20 campaign over Grand Mesa. I1, I2, I3 and I5, I6, I7 indicate the six InSAR pairs used for data assimilation and model evaluation respectively. The dates with green and blue tick mark represent days when the retrievals were used for assimilation in the data assimilation experiments.
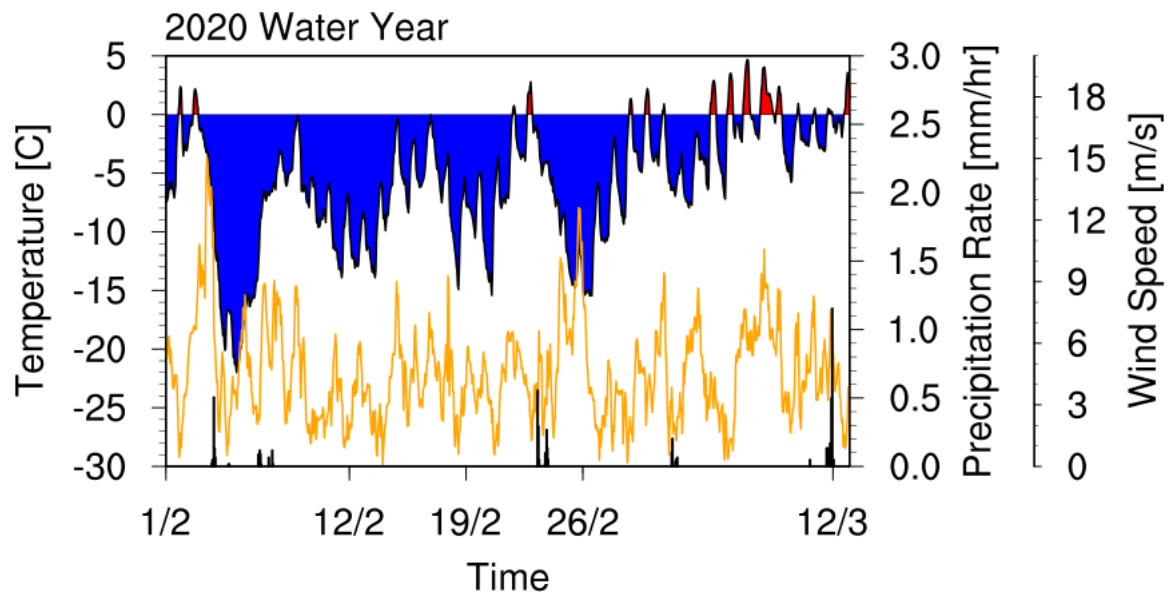
Figure 3: Meteorological data from atmospheric model for north-west GM subdomain showing air temperature (blue/red), wind speed (orange) and precipitation rate (bar plot). The time axis highlights the dates when the L-band UAVSAR flight data were available for SnowEx'20 campaign.

919

920
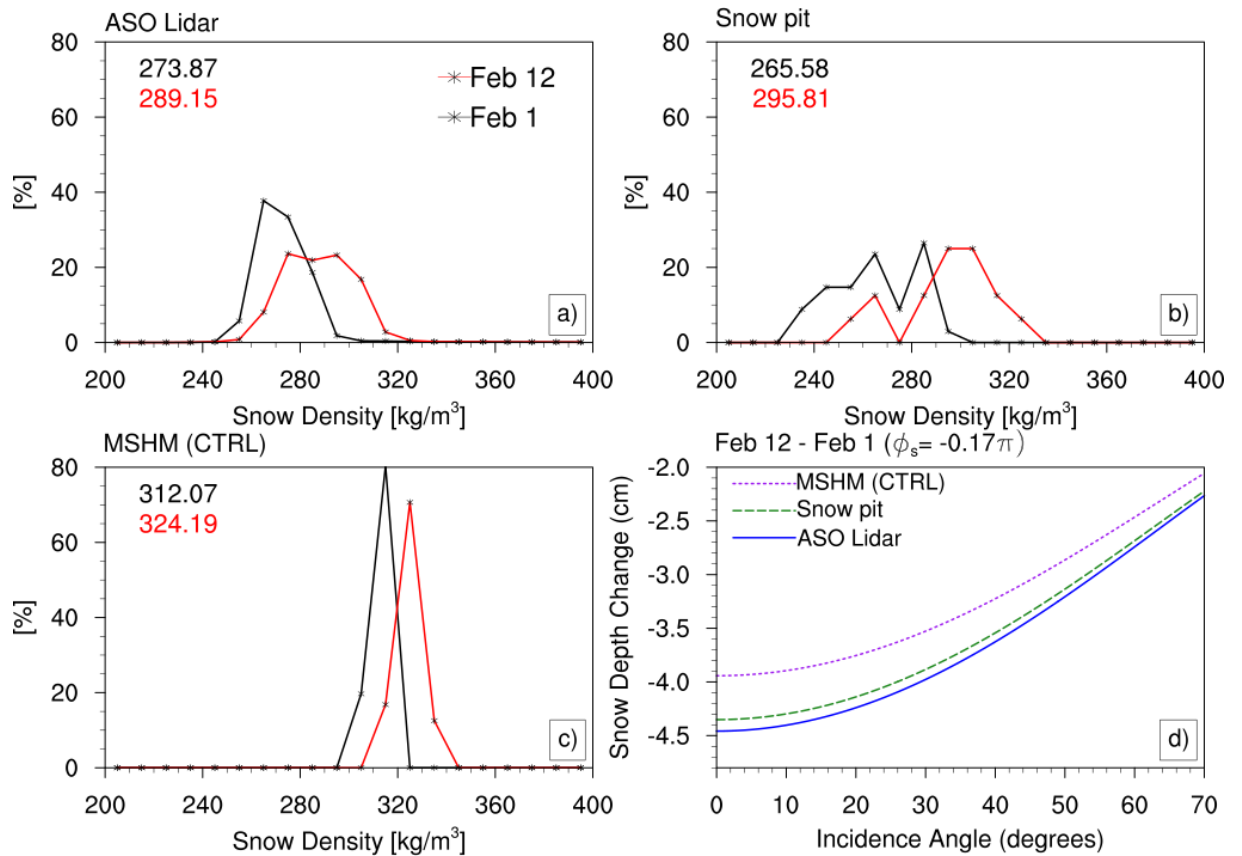
921   **Figure 4: a-c)** Snow density distribution at two different dates from the ASO Lidar data,

922   snow pit measurements (Intensive Observation Period, gray solid markers in Fig. 1)

923   and MSHM control run. **d)** Impact of snow density on the L-band InSAR retrieval of

924   snow depth change between the two dates as a function of incidence angle for a fixed

925   change in phase due to snowpack ($\emptyset_s = 0.17\pi$). The dates for ASO Lidar in actual are

926   Feb 1/2 and Feb 13. We use Feb 1 and Feb 12, due to availability of InSAR phase data

927   for these dates.

928

929
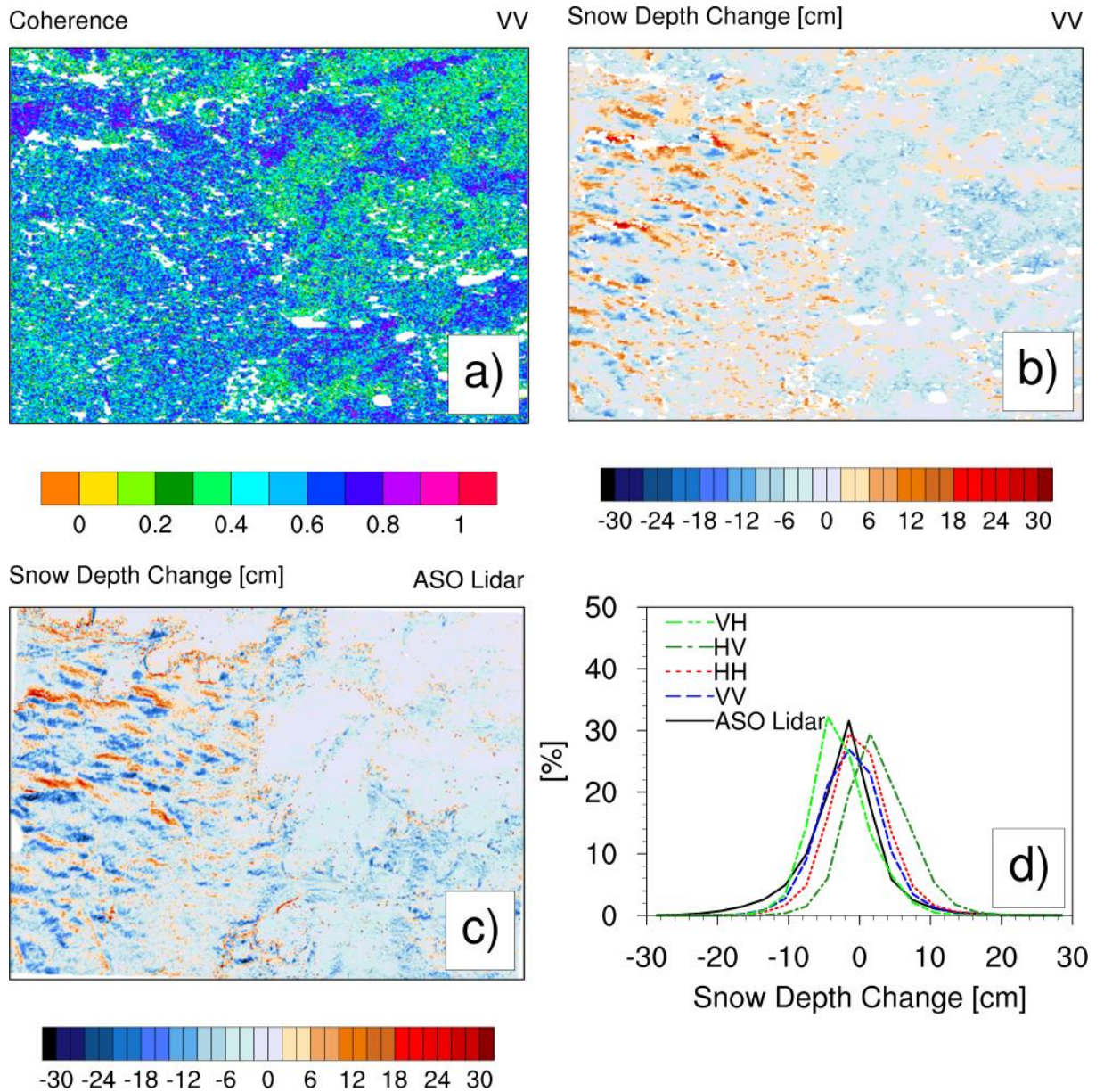
932 **Figure 5: a)** Spatial pattern of coherence from L-band VV polarization InSAR retrieval

933 for north-west GM subdomain. **b)** Estimated spatial pattern of snow depth changes

934 from the same retrieval. **c)** Spatial pattern of snow depth change from ASO Lidar data

935 (Feb 1/2–13). **d)** Distribution of change in snow depth for ASO Lidar and InSAR

936 retrievals for VV, HH, HV and VH polarizations. The InSAR retrievals were obtained

937 from UAVSAR flight pairs for Feb 1 and Feb 12.

938
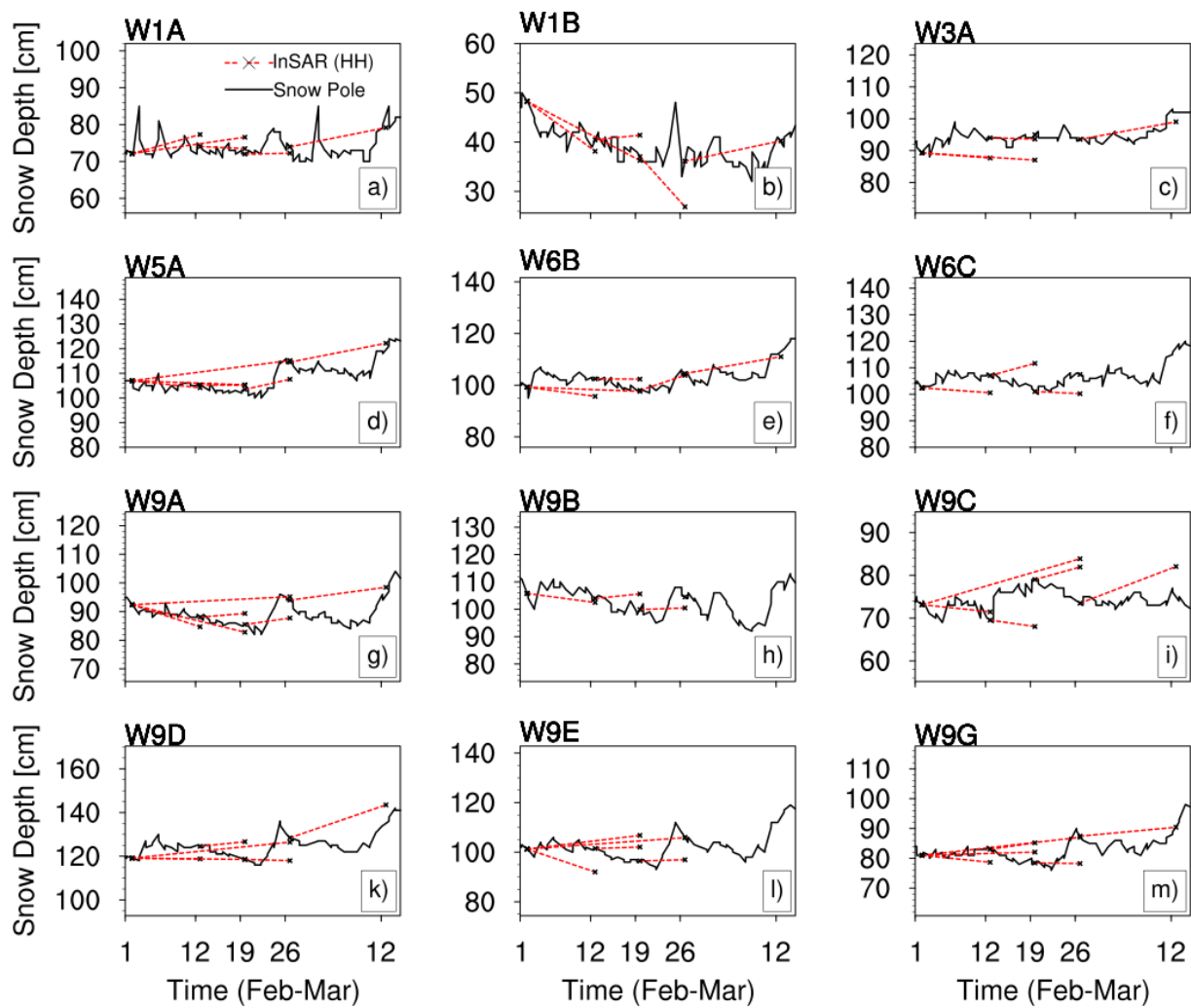
Figure 6: Comparison of L-band InSAR retrieval (HH polarization) of snow depth with Snow Pole measurements for locations with different landcover within the GM domain (**a-c:** Treeless; **d-f:** Sparse trees; **g-m:** Dense trees). For the InSAR retrieval, snow depth measurements from Snow Pole sites were used a reference for the repeat pass UAVSAR flight pairs.
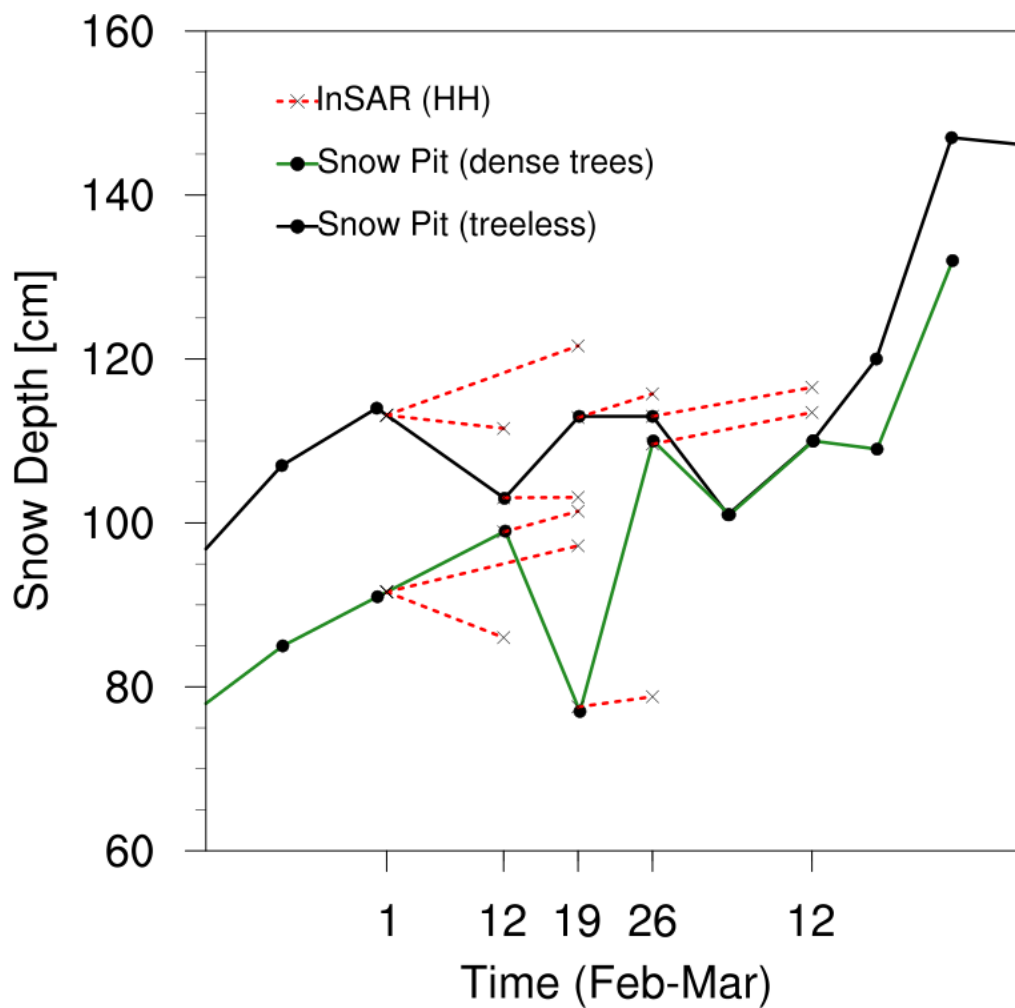
949 **Figure 7:** Comparison of L-band InSAR retrieval (HH polarization) of snow depth

950 with snow pit time-series measurements for two locations with different landcover

951 (treeless and dense trees) within the GM domain. For the InSAR retrieval, snow depth

952 measurements from snow pit site were used a reference for the repeat pass UAVSAR

953 flight pairs

954

955
956
957   **Figure 8:** Time series of modeled snow depth for CTRL, OL, DA and DAU run.

958 The dates when observation were assimilated are also shown by tick marks: DA (Feb

959 1) and DAU (Feb1, Feb 12 and Feb 26) are also shown by the tick marks. The

960 ensemble spread for OL, DA and DAU runs are shown by the dotted lines.

961
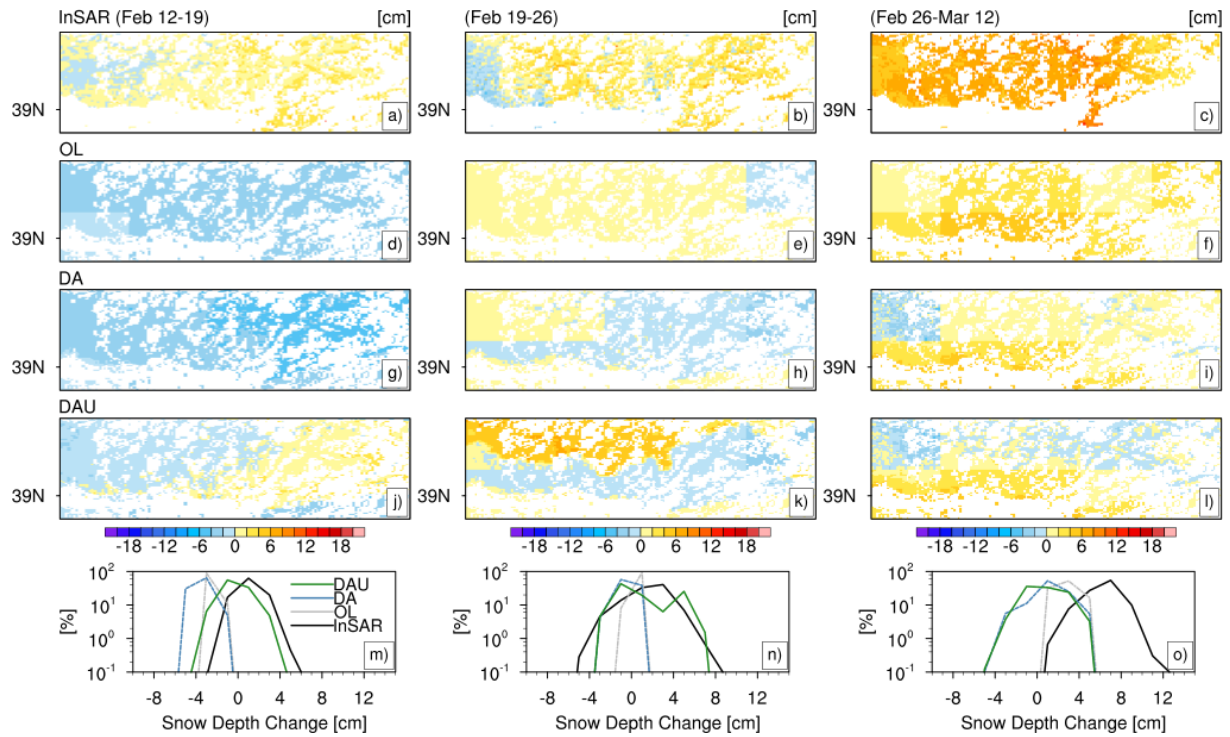
Figure 9: Spatial pattern and histogram of change in snow depth over the GM domain for Feb 12-19, Feb 19-26 and Feb 26-Mar 12: **a-c)** InSAR retrievals, **d-f)** ensemble averaged open loop run (OL), **g-i)** ensemble averaged data assimilation run with ASO Lidar data (DA), **j-l)** ensemble average data assimilation runs with ASO Lidar and referenced InSAR data (DAU), and **m-p)** frequency distribution of snow depth change for InSAR, OL, DA and DAU runs for respective pairs.